RESEARCH ARTICLE

Check for updates

Origin of the exceptional selectivity of NaA zeolite for the radioactive isotope $^{90}Sr^{2+}$†

Wenfeng Hao,‡[a] Nana Yan,‡[b] Miao Xie,‡[c] Xiaojun Yan,[d] Xiliang Guo,[d] Pu Bai,[e] Peng Guo, [b] Tao Cheng *[c] and Wenfu Yan *[a]

In this work, we reported an exceptionally high selectivity of a NaA zeolite (for which the framework type code of **LTA** was assigned by the Structure Commission of the International Zeolite Association) towards radioactive $^{90}Sr^{2+}$ and explained the origin of this high selectivity by combining structural Rietveld refinements and density functional theory (DFT) calculations. Nuclear wastewater with a $^{90}Sr^{2+}$ radioactive concentration of 400 Bq L^{-1} (7.75×10^{-2} ppt) and highly concentrated NaNO$_3$ and NH$_4$NO$_3$ (0.03 M Na$^+$ and 0.4 M NH$_4^+$, Na$^+$/$^{90}Sr^{2+}$ = 3.48×10^{10}, and NH$_4^+$/$^{90}Sr^{2+}$ = 4.64×10^{11}) was treated with NaA zeolite. The resultant $^{90}Sr^{2+}$ radioactive concentration was as low as 0.62 ± 0.12 Bq L^{-1}, close to the upper limit of ^{90}Sr-induced radioactive activity in drinking water, and the distribution coefficient, K_d, was as high as 421.56 ± 13.39 L g^{-1}. The NaA zeolite showed fast adsorption kinetics (*ca.* 5 min), high capture capacity (294.12 mg g^{-1}), a broad working pH range (4–12), and excellent radiation resistance. The crystallinity and performance of NaA zeolite were not affected by 1000 kGy ^{60}Co γ irradiation. Structural Rietveld refinements revealed that all Sr^{2+} ions are located at the center of the single 6-membered rings (*s6rs*) of the NaA zeolite. DFT calculations showed the free energy difference of exchanging different cations with Na$^+$ located in the 8-membered ring (*s8r*) of the NaA zeolite, and predicted the sequence of Sr^{2+}(−8.17 eV) > Ca^{2+}(−6.17 eV) > K$^+$(−2.13 eV) > Mg^{2+}(−1.94 eV) > NH$_4^+$(−0.65 eV) > Cs$^+$(−0.11 eV). The strong tendency of Sr^{2+} replacing Na$^+$ explains the exceptionally high selectivity of the NaA zeolite for $^{90}Sr^{2+}$ in high concentrations of Na$^+$ and NH$_4^+$. Along with the ion-exchange process, structural Rietveld refinements revealed that the Sr^{2+} ions at the *s8rs* center migrated to the *s6rs* center.

[a]*State Key Laboratory of Inorganic Synthesis and Preparative Chemistry, College of Chemistry, Jilin University, Changchun 130012, China. E-mail: yanw@jlu.edu.cn*
[b]*National Engineering, Research Center of Lower-Carbon Catalysis Technology, Dalian Institute of Chemical Physics, Chinese Academy of Sciences, Dalian 116023, China*
[c]*Institute of Functional Nano & Soft Materials (FUNSOM), Jiangsu Key Laboratory for Carbon-Based Functional Materials & Devices, Joint International Research Laboratory of Carbon-Based Functional Materials and Devices, Soochow University, 199 Ren'ai Road, Suzhou, 215123 Jiangsu, China. E-mail: tcheng@suda.edu.cn*
[d]*Division of Waste Disposal Technology, Waste Management Department, China Institute for Radiation Protection, Taiyuan 030006, Shanxi, China*
[e]*Luoyang Jalon Micro-Nano New Materials Co., Ltd, Luoyang 471900, China*

‡These authors contributed equally to this work.

1. Introduction

The *World Nuclear Industry Status Report 2021* reports that nuclear energy's share of global gross electricity generation was 10.1% in 2020 and it continues to increase. However, the rapid development of the nuclear energy industry and its projects leads to an increased chance of harmful fission product-radionuclides being released into the environment, seriously threatening aquatic life and human health.[1–5] Among these harmful fission products, ^{90}Sr is the most biohazardous species because of its high fission yield (5.73% with ^{235}U as fuel) and relatively long half-life (28.8 years). Due to the similarity in its chemical properties compared with Ca^{2+}, $^{90}Sr^{2+}$ readily accumulates in bones of humans and animals, causing blood and bone cancers through the emission of high energy beta rays.[4,6–8]

The US Environmental Protection Agency has set the upper limit of ^{90}Sr-induced radioactive activity in drinking water as 0.3 Bq L^{-1}, corresponding to 6.3×10^{-16} mol L^{-1} or 5.8×10^{-5} parts per trillion (ppt) of ^{90}Sr in terms of chemical concentration, suggesting that essentially all $^{90}Sr^{2+}$ must be removed from nuclear wastewater (*e.g.*, reprocessing liquid waste) before releasing it into the environment.[9] Even though $^{90}Sr^{2+}$ is present in the solution as a single component (*i.e.*, no competitive radioactive cations are present), its complete removal is still a huge challenge due to the extremely low concentration threshold. Moreover, an excess of many more competitive non-

6258 | *Inorg. Chem. Front.*, 2022, **9**, 6258–6270

This journal is © the Partner Organisations 2022

radioactive cations are also present in real nuclear wastewater. Accordingly, in real low-level radioactive wastewater from a domestic nuclear power plant with a $^{90}Sr^{2+}$ radioactive activity of 400 Bq L^{-1} (7.75×10^{-2} ppt), the concentration of NaNO$_3$ and NH$_4$NO$_3$ is 0.03 and 0.4 mol L^{-1}, respectively, corresponding to a Na$^+$/$^{90}Sr^{2+}$ ratio of 3.48×10^{10} and an NH$_4^+$/$^{90}Sr^{2+}$ ratio of 4.64×10^{11} in mol, respectively. The capture of the trace level radioactive $^{90}Sr^{2+}$ from highly salted nuclear wastewater produced from nuclear power plants is a huge challenge in low-level radioactive wastewater treatment. Moreover, the $^{90}Sr^{2+}$ removal system must be radiation-proof to eliminate potential safety hazards after solidification.

Several methods have been developed to remove $^{90}Sr^{2+}$, including adsorption,[5,10–12] solvent extraction,[13,14] chemical precipitation,[15,16] membrane filtration,[5,17,18] and bio-treatment.[19] Because the concentration of $^{90}Sr^{2+}$ is extremely low in nuclear wastewater, either adsorption *via* ion exchange or extraction with a strong binding site to $^{90}Sr^{2+}$ is the most efficient and energy-saving method.[1,20–26]

Various organic and inorganic absorbents have been employed to remove $^{90}Sr^{2+}$, including resins,[27,28] activated carbon,[29] natural minerals,[30,31] zeolites,[32,33] metal–organic frameworks (MOFs),[34,35] covalent organic frameworks (COFs),[36] *etc*. Compared with organic/polymer-based ion exchangers, inorganic ion exchangers are more affordable for large-scale applications. Meanwhile, their improved mechanical and thermal stability and excellent radiation resistance[37] make them more suitable in treating radioactive wastewater. Zeolites, which are types of microporous aluminosilicate crystals with negatively charged frameworks and ion-exchangeable counter-cations, with high ion exchange capacity, excellent thermal, mechanical, and radiation stability, and low price, are desirable candidates for nuclear waste treatment.[38] To date, zeolites with framework type codes of **LTA**, **GIS**, **CHA**, **MOR**, **FAU**, **MFI**, and ***BEA** have been investigated in their removal of radionuclides. Among them, **LTA** is the most promising adsorbent to selectively remove $^{90}Sr^{2+}$ ions.[39]

So far, most of the reported experiments involving zeolites have been focused on the adsorption of non-radioactive Sr^{2+} or the radioactive $^{90}Sr^{2+}$ at a concentration much higher than the ppt level when fewer competitive cations are present. In this study, we use NaA zeolite to capture at the ppt level radioactive $^{90}Sr^{2+}$ from nuclear wastewater with a $^{90}Sr^{2+}$ radioactive activity of 400 Bq L^{-1} (7.75×10^{-2} ppt) and high concentrations of NaNO$_3$ and NH$_4$NO$_3$ (0.03 M Na$^+$ and 0.4 M NH$_4^+$, corresponding to Na$^+$/$^{90}Sr^{2+}$ = 3.48×10^{10}, and NH$_4^+$/$^{90}Sr^{2+}$ = 4.64×10^{11}, respectively). NaA zeolite showed exceptionally high selectivity for the radioactive isotope of $^{90}Sr^{2+}$, fast adsorption kinetics (*ca.* 5 min), high capture capacity (294.12 mg g^{-1}), and a broad working pH range (4–12). The origin of high Sr^{2+} selectivity in NaA zeolite was investigated by combining structural Rietveld refinements and density functional theory (DFT) calculations. The superior selectivity, coupled with the ultralow cost and environmentally benign nature, renders NaA zeolite a promising candidate in nuclear wastewater management.

2. Experimental section

2.1 Synthesis

2.1.1 Chemicals and materials. Commercial NaA zeolite powder was obtained from Luoyang Jalon Micro-Nano New Materials Co., Ltd. Colloidal silica (Ludox® AS-40, 40%) was obtained from Aldrich. Triethanolamine (TEA), potassium nitrate, magnesium nitrate, and NaAlO$_2$ were acquired from Sinopharm Chemical Reagent Co., Ltd. Sodium hydroxide and nitric acid were obtained from Beijing Chemical Works. Sodium nitrate was obtained from Tianjin Guangfu Fine Chemical Research Institute. Calcium nitrate was obtained from Tianjin Fuchen Chemical Reagents Factory. Strontium chloride (guaranteed reagent) was obtained from Shanghai Macklin Blochemical Co., Ltd. The chemicals were purchased and used without further purification.

2.1.2 Synthesis of NaA single crystals for Rietveld refinements. NaA zeolite single crystals, which possess shapes of edge-truncated cubes and sizes of 15–20 μm in edge length, have been synthesized with a starting mixture having a molar composition of 1.7 Na$_2$O : Al$_2$O$_3$: 0.7 SiO$_2$: 165 H$_2$O : 6.1 TEA.[40] The initial mixture was prepared as follows: NaOH and NaAlO$_2$ were dissolved in deionized water to form a clear solution. TEA was thoroughly dispersed in the solution, followed by slow addition of colloidal silica. The resultant mixture was stirred at 0 °C for 1 h to ensure homogeneity, then transferred into a Teflon-lined stainless steel autoclave, and heated at 85 °C for 21 d. The product was separated by filtration, washed 3 times with deionized water and dried at 353 K overnight. The elemental analysis confirmed that the Si/Al ratio of NaA single crystals was 1, the same as that of the NaA zeolite powder from Luoyang Jalon Micro-Nano New Materials Co., Ltd.

2.2 Characterization

Powder X-ray diffraction (PXRD) data were recorded on a Rigaku D/Max 2550 X-ray diffractometer with Cu-Kα radiation (λ = 1.5418 Å) at 50 kV and 200 mA. Thermogravimetric analysis (TGA) was performed using a TA TGA Q500 in an air atmosphere with a heating rate of 10 °C min^{-1} from ambient temperature to 800 °C. The morphology was investigated with field emission scanning electron microscopy (SEM, JSM-7800F). The elemental composition of solid samples was analysed using an Oxford X-MAX 80 energy dispersive spectrometer (EDS). The chemical composition of the solutions was determined with inductively coupled plasma (ICP) analyses carried out on a Thermo Fisher Scientific iCAP7600 DUO instrument. PXRD data for Rietveld refinements were collected on a STOE STADI P ESSENTIAL X-ray diffractometer equipped with a Mython II detector in the Debye–Scherrer mode with Cu Kα1 radiation (λ = 1.5406 Å). The radioactive activity of the solution was measured using a Low background alpha beta measuring instrument LB4110 (ShangHai Ergonomics Detecting Instrument Co., Ltd). The γ-ray radiation was provided by a ^{60}Co radiation source with a radiation dose rate no higher than 2000 Gy h^{-1}. The total radiation time was 500 h, and the total radiation dose was 1000 kGy. The

This journal is © the Partner Organisations 2022

Inorg. Chem. Front., 2022, **9**, 6258–6270 | **6259**

zeta potential was measured by a Zetasizer-Nano ZS (Malvern Instruments Ltd).

2.3 Radioactive $^{90}Sr^{2+}$ adsorption

The assessment of NaA zeolite for $^{90}Sr^{2+}$ removal was conducted using a solution with a pH of 8 and a radioactive activity of 400 Bq L^{-1} (7.75×10^{-2} ppt), 0.03 M Na$^+$ (2500 ppm NaNO$_3$), and 0.4 M NH$_4^+$ (32 000 ppm NH$_4$NO$_3$), corresponding to a Na$^+$/$^{90}Sr^{2+}$ molar ratio of 3.48×10^{10} and an NH$_4^+$/$^{90}Sr^{2+}$ molar ratio of 4.64×10^{11}, respectively. The experiments were conducted with solid/liquid ratios of 1/20, 1/100, 1/500, 1/1000, 1/2000, and 1/5000 in g mL^{-1} by adding pre-weighed NaA zeolite powder into 20 mL of the radioactive solution.

2.4 Rietveld refinements

Two NaA zeolites with calculated exchange degrees of 50 and 100% for Sr^{2+}, respectively, were prepared with controlled initial concentrations of Sr^{2+}. In detail, 0.2791 g (50%) or 0.5582 g (100%) of SrCl$_2$ was added to 50 mL of deionized water containing 1.0 g NaA zeolite. The resultant slurry was stirred for 12 h at 25 °C. The product was separated by filtration and dried at 80 °C. The composition of the resultant product was $|Na_{31.51}Sr_{23.99}Ca_{6.76}H_{2.99}|[Si_{96}Al_{96}O_{384}]$ (denoted as NaA-Sr-1) and $|Na_{17.00}Sr_{29.64}Ca_{6.03}H_{7.66}|[Si_{96}Al_{96}O_{384}]$ (denoted as NaA-Sr-2), respectively. The actual exchange degree for the two NaA zeolites was 49.97 and 61.75%, respectively. Ca^{2+} ions as impurities come from the raw material SrCl$_2$. Before collecting the PXRD data for Rietveld refinements, both samples were transferred into a capillary with a diameter of 0.2 mm and then dehydrated at 300 °C for 12 h. Subsequently, the capillary was sealed with wax and measured with a 2θ angle range of 5–120°, step size of 0.015°, and a total counting time of 24 h at ambient temperature.

2.5 Theoretical calculations

The periodic DFT calculations were carried out using VASP (version 5.4.4).[41,42] The DFT calculations were performed under the Perdew, Burke, and Ernzerhof (PBE)[43] flavour of density functional theory (DFT) with the post-stage van der Waals attraction, DFT-D3 with Becke–Johnson damping.[44] The projector augmented wave (PAW) method[45,46] was used to account for core–valence interactions. The kinetic energy cutoff for plane wave expansions was set to 400 eV, and reciprocal space was sampled with only gamma point. The energy convergence criterion is 1×10^{-5} eV when solving the electronic wave function. The Methfessel–Paxton smearing of the second order with a width of 0.1 eV was applied. All geometries were considered converged when the maximum force is less than 3×10^{-2} eV Å^{-1}. All atoms of the *lta* cage extracted from the NaA zeolite were fixed, while the metal cations and H$_2$O molecules were relaxed during the calculations.

The cluster DFT calculations were performed using the Gaussian (2016 Revision A.03) program.[47] The B3LYP hybrid functional was employed.[48] The LanL2DZ basis sets with a quasi-relativistic pseudopotential were used to describe the K, Cs, Mg, Ca, and Sr elements, and the split valence basis set

6–21 was employed for the other elements (H, N, O, Na, Al, and Si elements). D3 dispersion correction was included to take into account the dispersion interaction. Solvation effects were considered using the continuum solvent model, SMD, with parameters settings for water.[49]

In this work, a cluster model with constraints to represent the zeolite crystal structure was employed to simulate the ion-exchange process as observed experimentally. The initial structure model of the *lta* cage of NaA zeolite was obtained from the high symmetry refined structures that contains an *lta* cage, six single 8-rings (*s8r*), and eight single 6-rings (*s6r*). The center of each *s8r* and *s6r* is occupied by Na$^+$, leading to 14 Na$^+$ ions in the simulation model. Moreover, the breaking bonds of terminal oxygen were saturated with hydrogen atoms, leading to a formula of $[Na_{14}Al_{24}Si_{24}O_{72}(OH)_{48}]^{10-}$. Although the single defect method has an advantage in avoiding the ambiguity in defining the reference states,[50,51] the solvation effect can be more easily included in the direct simulation of the aqueous exchange process. To simulate the ion-exchange process under the experimental conditions, a model with 20 water molecules inside the *lta* cage was established according to the experimental analysis of synthetic and hydrated NaA zeolite.[52,53] The model with explicit water molecules has the formal formula of $[Na_{14}Al_{24}Si_{24}O_{72}(OH)_{48} \cdot 20H_2O]^{10-}$, and the atomic coordinates are provided in Fig. S1.† The metal cations were all solvated by water molecules. Six water molecules were bound to Sr^{2+} and Na$^+$ cations to simulate the first solvation shell.[54,55]

2.6 Batch adsorptions

2.6.1 Influence of ion-exchange time. In the batch adsorption experiments, 0.01 g of NaA zeolite was added to 10 mL of SrCl$_2$ solutions with an initial concentration of 100 mg L^{-1} and a pH of 6.7 at 25 °C. A series of adsorption experiments were performed by varying the stirring times to be 0.25, 0.5, 1, 2, 3, 4, 5, 6, 7, 8, 9, and 10 minutes. The solutions were filtered with a polyethersulfone (PES) membrane (diameter 13 mm, pore size 0.22 μm). Adsorption capacity (Q_e), removal efficiency (R), and distribution coefficient K_d (mL g^{-1}) were calculated using the following mass balance equations:[56]

$$R(\%) = \frac{C_i - C_e}{C_i} \times 100$$

$$Q_e = \frac{(C_i - C_e) \times V}{m}$$

$$K_d = \frac{C_i - C_e}{C_e} \times \frac{V}{m}$$

where C_i and C_e are the initial and the equilibrium concentrations of Sr^{2+} (mg L^{-1}), respectively, V is the solution volume (L), and m is the adsorbent mass (g).

The ICP-MS analyses had an uncertainty of ±10%, but our repeatability tests indicated that this uncertainty was often within ±5%. All samples were analyzed three times. The average values were calculated, and the corresponding errors were estimated from the two samples' standard deviations of each triplicate set.

6260 | *Inorg. Chem. Front.*, 2022, **9**, 6258–6270

This journal is © the Partner Organisations 2022

2.6.2   Influence of adsorbent dosage. A series of adsorption experiments were performed by varying the amount of adsorbent dosages (0.20, 0.10, 0.04, 0.02, and 0.01 g of NaA zeolite powder per 20 mL of Sr^{2+} solution) under stirring for 12 h at pH 6.7, corresponding to solid/liquid ratios of 1/100, 1/200, 1/500, 1/1000, and 1/2000 in g mL^{-1}.

2.6.3   Influence of pH. A series of solutions of Sr^{2+} with a pH of 3–12 were prepared by first adjusting with 1.0 M HNO_3 and NaOH solutions and then with 0.1 M HNO_3 and NaOH solutions when the pH of the solution was close to the pre-set value. Adsorption experiments were conducted by mixing 0.01 g of NaA zeolite with 10 mL of Sr^{2+} solution with a concentration of 100 mg L^{-1} under stirring for 12 h at 25 °C.

2.6.4   Influence of initial concentration of Sr^{2+} solutions. The concentrations of Sr^{2+} were varied from 50 to 400 mg L^{-1} with an interval of 50 mg L^{-1}. Adsorption experiments were conducted by mixing 0.01 g of NaA zeolite with 10 mL of Sr^{2+} solution under stirring for 12 h at 25 °C.

2.6.5   Influence of competitive cations (selectivity). The concentration of Sr^{2+}, Na^+, K^+, Mg^{2+}, and Ca^{2+} was 100 mg L^{-1}. Adsorption experiments were conducted by mixing 0.01 g of NaA zeolite with 10 mL of mixed solution under stirring for 12 h at 25 °C.

The concentration of Sr^{2+} was 100 mg L^{-1}, while that of competitive cations Na^+, K^+, Mg^{2+}, and Ca^{2+} was set as 0.1, 0.2, 0.3, 0.4, or 0.5 mol L^{-1}. Adsorption experiments were conducted by mixing 0.01 g of NaA zeolite with 10 mL of Sr^{2+} solution under stirring for 12 h at 25 °C.

3.   Results and discussion

3.1   Characterization studies of NaA zeolite

The XRD patterns of the as-synthesized NaA single crystals, the commercial NaA powder, and the 1000 kGy ^{60}Co γ-irradiated commercial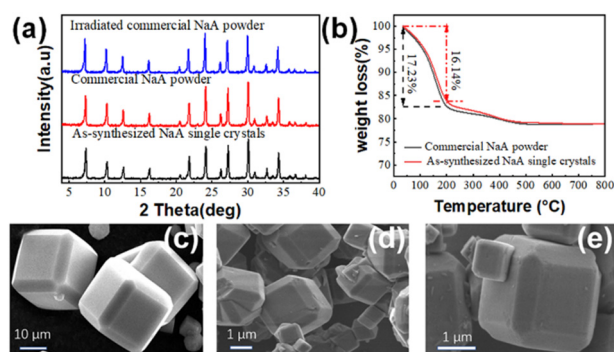 NaA powder are shown in Fig. 1(a), which fit well with each other, indicating that the as-synthesized NaA in the form of single crystals is a pure phase and both commercial NaA powder and as-synthesized NaA single crystals are radiation resistant. TG curves of the NaA powder and the NaA single crystals are shown in Fig. 1(b), demonstrating the presence of physically adsorbed H_2O in both samples (17.23 wt% for NaA powder and 16.14 wt% for NaA single crystals), which will be taken into account in the subsequent calculation of the adsorption capacity for Sr^{2+}. The SEM image in Fig. 1(c) shows that the as-synthesized NaA single crystals possess the shape of edge-truncated cubes with sizes of 15–20 μm in edge length. Fig. 1(d) shows the SEM image of the commercial NaA powder, showing that the commercial NaA powder also possesses the shape of edge-truncated cubes but with a reduced size of 2 μm in edge length. After irradiation, the shape of the crystals of commercial NaA powder is maintained, as shown in Fig. 1(e).

3.2   Adsorption of radiative $^{90}Sr^{2+}$

The radioactive activity of $^{90}Sr^{2+}$ in the solution was 400 Bq L^{-1}, which corresponds to a concentration of 7.75×10^{-2} ppt or 8.62×10^{-13} M. The concentration of Na^+ and NH_4^+ was 0.03 M (2500 ppm $NaNO_3$) and 0.4 M (32 000 ppm NH_4NO_3), respectively, corresponding to a $Na^+/^{90}Sr^{2+}$ molar ratio of 3.48×10^{10} and an $NH_4^+/^{90}Sr^{2+}$ molar ratio of 4.64×10^{11}, respectively. 20 mL of radioactive solution was mixed with various doses of NaA powder to meet the solid/liquid ratios of 1/20, 1/100, 1/500, 1/1000, 1/2000, and 1/5000 in g mL^{-1}. The removal efficiencies under various solid/liquid ratios and the corresponding distribution coefficients are shown in Fig. 2 and the detailed values are listed in Table S1.†

As shown in Fig. 2, the $^{90}Sr^{2+}$ removal efficiency reached a maximum value of 99.83% at the solid–liquid ratio of 1 : 20 g mL^{-1}, and the final radioactive activity of ^{90}Sr was 0.63 ± 0.12 Bq L^{-1}, which is very close to the upper limit of 0.3 Bq L^{-1} set by the US Environmental Protection Agency for ^{90}Sr-induced radioactive activity in drinking water. With a decreasing sorbent dosage, the removal efficiency of ^{90}Sr decreased very slightly. At the solid/liquid ratio of 1/2000 in g mL^{-1}, the
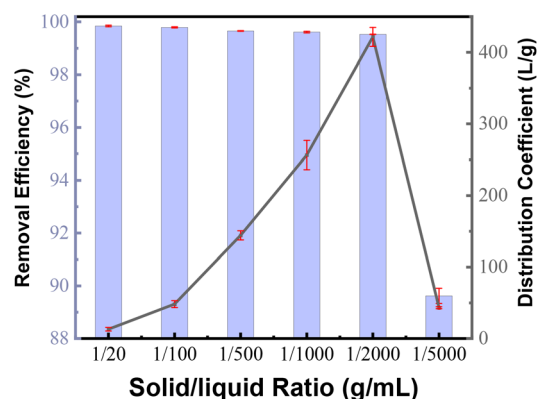

Fig. 1   (a) XRD patterns of the as-synthesized NaA single crystals, commercial NaA powder, and 1000 kGy ^{60}Co γ-irradiated commercial NaA powder; (b) TG curves of the as-synthesized NaA single crystals (red) and the commercial NaA powder (black); (c) SEM image of the as-synthesized NaA single crystals; (d) SEM image of the commercial NaA powder, and (e) SEM image of the 1000 kGy ^{60}Co γ-irradiated commercial NaA powder.

Fig. 2 $^{90}Sr^{2+}$ removal efficiencies of NaA powder with various solid/liquid ratios and the corresponding distribution coefficients in L g^{-1}.

Table 1 Removal performance for $^{90}Sr^{2+}$ using zeolite NaA and other adsorbents

Adsorbent	Initial concentrations	Competitive ions' concentration (ppm)	$n(M)^{n+}/n(Sr)^{2+}$	Performance	Ref.
Resorcinol formaldehyde polycondensate resin	10 ppm	Na^+: 20 000, K^+: 850	Na^+: Sr^{2+} = 7619.13	Adsorption capacity: 14.90 mg g^{-1}	28
			K^+: Sr^{2+} = 190.97		
Sodium nonatitanate powder	77 730 Bq L^{-1} (1.51 × 10^{-5} ppm)	Na^+: 360, Ca^{2+}: 67	Na^+: Sr^{2+} = 9.33 × 10^7	After adsorption: 8530 Bq L^{-1}	57
		A little Mg^{2+} and K^+	Ca^{2+}: Sr^{2+} = 9.98 × 10^6	K_d = 16 225 mL g^{-1}	
$Na_2Ti_nO_{2n+1}/SiO_2$	1 ppm	Na^+: 10 000, K^+: 400, Ca^{2+}: 5, and Mg^{2+}: 5	Na^+: Sr^{2+} = 38 095.65	Adsorption capacity: 4.37 mg g^{-1}	58
			K: Sr^{2+} = 898.67 Ca^{2+}: Sr^{2+} = 10.95 Mg^{2+}: Sr^{2+} = 18.02		
$K_2Ti_6O_{13}/SiO_2$	1 ppm	Na^+: 10 000, Ca^{2+}: 10, Mg^{2+}: 1	Na^+: Sr^{2+} = 38 095.65	Adsorption capacity at breakthrough point: 0.176 mg g^{-1} Column test	59
			Ca^{2+}: Sr^{2+} = 21.90 Mg^{2+}: Sr^{2+} = 3.60		
Layered vanadosilicate	28 100 Bq L^{-1} (5.4 × 10^{-6} ppm)	Na^+: 46 000	Na^+: Sr^{2+} = 3.33 × 10^{10}	K_d = 536 mL g^{-1}	9
	32 100 Bq L^{-1} (6.2 × 10^{-6} ppm)	Na^+: 115 000	Na^+: Sr^{2+} = 7.23 × 10^{10}	K_d = 119 mL g^{-1}	
Zeolite A	77 730 Bq L^{-1} (1.51 × 10^{-5} ppm)	Na^+: 360, Ca^{2+}: 67	Na^+: Sr^{2+} = 9.33 × 10^7	After adsorption: 3400 Bq L^{-1}	57
		A little Mg^+ and K^+	Ca^{2+}: Sr^{2+} = 9.98 × 10^6	K_d = 43 723 mL g^{-1}	
Macroporous zeolite A monolith	28 520 Bq L^{-1} (5.5 × 10^{-6} ppm)	Na^+: 9600, K^+: 400, Ca^{2+}: 400, Mg^{2+}: 1200	Na^+: Sr^{2+} = 6.83 × 10^9	Adsorption capacity at breakthrough point: 1.2 ng g^{-1}	60
			K^+: Sr^{2+} = 1.68 × 10^8 Ca^{2+}: Sr^{2+} = 1.64 × 10^8 Mg^{2+}: Sr^{2+} = 8.07 × 10^8	Column test	
Zeolite NaA	**400 Bq L^{-1} (7.75 × 10^{-2} ppt)**	**Na^+: 2500**	**Na^+: Sr^{2+} = 3.48 × 10^{10}**	**After adsorption: 1.89 Bq L^{-1}**	**This work**
		NH_4^+: 32 000	**NH_4^+: Sr^{2+} = 4.64 × 10^{11}**	**K_d = 421.56 ± 13.39 L g^{-1}**	

removal efficiency was as high as 99.53 ± 0.01%, corresponding to a K_d of 421.56 ± 13.39 L g^{-1}. According to the data reported so far on the adsorptive removal of $^{90}Sr^{2+}$ (Table 1), NaA zeolite shows the best capture performance for the removal of $^{90}Sr^{2+}$ from low-level radioactive liquid waste even under NH_4^+- and Na^+-rich conditions and low solid/liquid ratio of 1/2000 in g mL^{-1}, which makes NaA zeolite a promising candidate for nuclear wastewater management. However, at the solid/liquid ratio of 1/5000 in g mL^{-1}, the removal efficiency dropped to 89.62 ± 0.29%, corresponding to a K_d of 43.19 ± 1.34 L g^{-1}. These results show that the appropriate solid/liquid ratio is 1/2000 in g mL^{-1}.

3.3 Rietveld refinements

The NaA zeolite crystallizes in the cubic system with the space group of $Fm\bar{3}c$. From a topological point of view, each sodalite (sod) cage connects with six double 4-rings (d4rs), while each d4r is linked with two sod cages. In this case, the larger lta cages surrounded by smaller sod cages and d4rs are constructed. Meanwhile, all lta cages are connected through the s8r openings.[52] To reveal the origin of the exceptional selectivity of NaA zeolite for $^{90}Sr^{2+}$, we first conducted the structural Rietveld refinements for Sr^{2+} partially exchanged NaA (NaA-Sr-1 and NaA-Sr-2) since the concentration of $^{90}Sr^{2+}$ in low-level radioactive liquid waste is extremely low and the $^{90}Sr^{2+}$ can only partially replace the Na^+ in NaA via ion-exchange. Rietveld

refinements may provide us with the locations of Sr^{2+} after the adsorption.

Taking the NaA-Sr-1 sample as an example to illustrate the process of Rietveld refinements in detail, the profile fitting was first of all performed to identify the experimental unit cell parameters and check the phase purity. Then, the bond lengths and bond angles of the framework against the angle and distance restraints were further optimized. After that, the scale factors between the simulated PXRD data of the optimized framework and the experimental PXRD data were obtained against the high angle PXRD data (2θ: 60°–120°), where extra-framework species in the channels or cavities have a negligible effect. Subsequently, the electron difference density map can be calculated by applying the scale factors to full ranges (Fig. 3).

Since dehydrating the sample has eliminated the interference from water, the electron density map shows the positions of the cations in NaA-Sr-1. It turns out that all cations are located in the single 6-rings (s6r) of the lta cage, as shown in Fig. 4. It is worth noting that there are non-ignorable Ca^{2+} cations in NaA-Sr-1 with a unit cell composition of $|Na_{31.51}Sr_{23.99}Ca_{6.76}H_{2.99}|[Si_{96}Al_{96}O_{384}]$, which was confirmed by EDS results. Fig. 4 illustrates that the final refined locations of Na^+, Sr^{2+}, and Ca^{2+} are in the s6r of the lta cage. Crystallographic details of Rietveld refinements are provided in Table S2.†

6262 | *Inorg. Chem. Front.*, 2022, **9**, 6258–6270

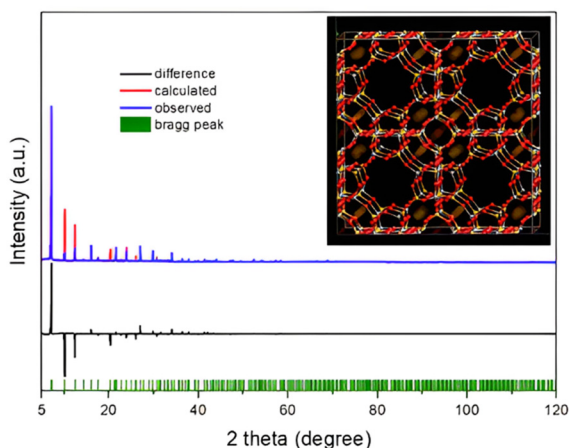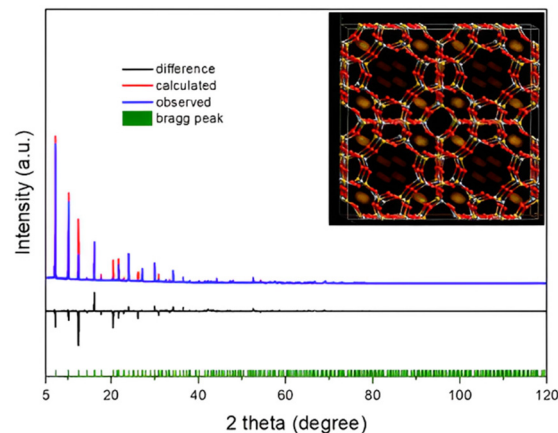This journal is © the Partner Organisations 2022

Fig. 3 Plots for locating cations in NaA-Sr-1 by applying the appropriate scale factor to the whole pattern. The inset is the difference electron density map to locate the initial positions through Rietveld refinements. The observed, calculated, and difference curves are in blue, red, and black, respectively. The vertical bars indicate the positions of Bragg peaks ($\lambda = 1.5406$ Å).

Fig. 4 Crystallographic structure of NaA-Sr-1. All cations Na$^+$, Sr^{2+}, and Ca^{2+} are located in the single 6-rings (s6r) of the lta cage (highlighted by the red circle).

Fig. 5 Plots for locating cations in NaA by applying the appropriate scale factor to the whole pattern. The inset is the difference electron density map to locate the initial positions through Rietveld refinements. The observed, calculated, and difference curves are in blue, red, and black, respectively. The vertical bars indicate the positions of Bragg peaks ($\lambda = 1.5406$ Å).
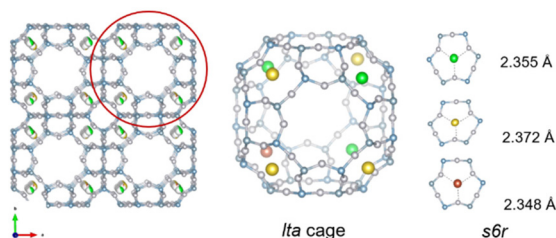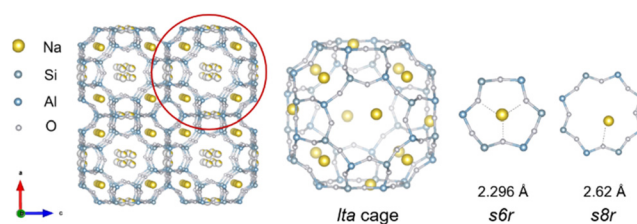

Fig. 6 Crystallographic structure of NaA. Na$^+$ cations are distributed in the s6r and the single 8-rings (s8r) of the lta cage (highlighted by the red circle).

Furthermore, the locations and occupancies of cations in NaA-Sr-2 are both determined by the same method, which has a higher Sr^{2+} exchange degree than that for NaA-Sr-1. Na$^+$, Sr^{2+}, and Ca^{2+} in NaA-Sr-2 are also located in the s6r of the lta cage, as shown in Fig. S2,† and its unit cell composition is |Na$_{17.00}$Sr$_{29.64}$Ca$_{6.03}$H$_{7.66}$||Si$_{96}$Al$_{96}$O$_{384}$].

To investigate the migration of cations, Rietveld refinements were also performed on the parent NaA zeolite. The electron density map of NaA in Fig. 5 shows that Na$^+$ cations are distributed in the s6r and the s8r of the lta cage. The final refined result of NaA is illustrated in Fig. 6, and the refined unit cell composition is |Na$_{88}$H$_8$||Si$_{96}$Al$_{96}$O$_{384}$].

According to the results of Rietveld refinements as mentioned above, the Sr^{2+} ions are exclusively located in the s6r. However, the detailed exchange mechanism needs to be further investigated by combining the theoretical calculations.

3.4 Theoretical calculations of the ion-exchange of Na$^+$ with Sr^{2+} in NaA zeolite

Explicitly hydrated cations are considered in the simulation to better describe the ion-exchange process in solution. Six water

molecules are placed around Na$^+$, K$^+$, Cs$^+$, Mg^{2+}, Ca^{2+}, and Sr^{2+} ions, and four water molecules are set around the NH$_4^+$ ion, because such hydration structures are those generally accepted to correctly reproduce the hydration properties of various ions.[54,61] The interaction energies between the framework and the Na$^+$ at the center of the s6r or the s8r are obtained from DFT calculations. The results in Fig. 7 show that the energy of Na$^+$ dissociation from s8r is −4.89 eV, compared with −3.15 eV from the s6r. Thus, DFT calculations indicate the ion-exchanged cations substituting for Na$^+$ in the s8r is easier. The potential energies of various cations substituting for Na$^+$ in the s8r are listed in Table 2. For alkali metal cations, DFT calculations indicate that Cs$^+$ has the weakest interaction energy of −0.11 eV, while that of K$^+$ is −2.13 eV.

For alkaline earth metal ions, the interaction energies follow the order of Mg^{2+} (−1.94 eV) < Ca^{2+} (−6.17 eV) < Sr^{2+} (−8.17 eV). Additionally, the interaction energy for NH$_4^+$ is the smallest (∼−0.65 eV), which can explain non-priority ion-exchanges occurring at extremely high NH$_4^+$ concentrations.

Under experimental conditions, NaA zeolite is in solution. To better describe the ion-exchange process of Sr^{2+} into NaA zeolite, we constructed a model with 20 water molecules inside
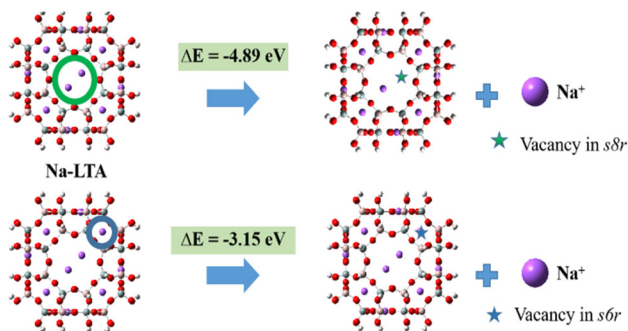
This journal is © the Partner Organisations 2022

Inorg. Chem. Front., 2022, **9**, 6258–6270 | **6263**

Fig. 7 Molecular structures of the $Na_{14}Al_{24}Si_{24}O_{72}(OH)_{48}$ *lta* cage (Na-LTA model) and the dissociation energies of Na^+ in the center of *s8r* and *s6r* in the Na-LTA model.

hydrated ions of $Na^+ \cdot (H_2O)_6$ and $Sr^{2+} \cdot (H_2O)_6$ are shown in Table S3†), and the detailed ion-exchange energies are summarized in Table 3.

As shown in Fig. 8, the first $Sr^{2+} \cdot (H_2O)_6$ is adsorbed *via* ion-exchange along with the dissociation of two Na^+ ions at an *s8r*'s center with ion-exchange energy of -7.30 eV. One *s8r* center is occupied by a Sr^{2+}, while the other one is empty (denoted as LTA-$Sr_{(8)}$). When the second $Sr^{2+} \cdot (H_2O)_6$ is adsorbed, the Sr^{2+} ion is directly located at the unoccupied *s8r* center, and two additional Na^+ ions are dissociated from the *s8r*'s center (denoted as LTA-$2Sr_{(8)}$). The ion-exchange energy for this step is -5.31 eV. Subsequently, the third $Sr^{2+} \cdot (H_2O)_6$ ion is adsorbed at the *s8r* center, and the last two Na^+ at

Table 2 Interaction energies (in eV) of Na^+ in the *s8r* of the *lta* cage exchanging with various cations

Adsorption reaction	ΔE (eV)
LTA + $2H_2O$ + $NH_4^+ \cdot (H_2O)_4 \rightarrow$ LTA-NH_4 + $Na^+ \cdot (H_2O)_6$	-0.65
LTA + $K^+ \cdot (H_2O)_6 \rightarrow$ LTA-K + $Na^+ \cdot (H_2O)_6$	-2.13
LTA + $Cs^+ \cdot (H_2O)_6 \rightarrow$ LTA-Cs + $Na^+ \cdot (H_2O)_6$	-0.11
LTA + $6H_2O$ + $Mg^{2+} \cdot (H_2O)_6 \rightarrow$ LTA-Mg + $2Na^+ \cdot (H_2O)_6$	-1.94
LTA + $6H_2O$ + $Ca^{2+} \cdot (H_2O)_6 \rightarrow$ LTA-Ca + $2Na^+ \cdot (H_2O)_6$	-6.17
LTA + $6H_2O$ + $Sr^{2+} \cdot (H_2O)_6 \rightarrow$ LTA-Sr + $2Na^+ \cdot (H_2O)_6$	-8.17

the *lta* cage extracted from NaA zeolite according to the experimental analysis of synthetic and hydrated NaA zeolite (Fig. S1†). We calculated the ion-exchange pathways of $Sr^{2+} \cdot (H_2O)_6$ as shown in Fig. 8 (the formation energies of the

Table 3 The calculated ion-exchange energies for adsorption of six $Sr^{2+} \cdot (H_2O)_6$ ions into NaA zeolite in sequence

Adsorption reaction pathway	ΔE (eV)
LTA + $6H_2O$ + $Sr^{2+} \cdot (H_2O)_6 \rightarrow$ LTA-$Sr_{(8)}$ + $2Na^+ \cdot (H_2O)_6$	-7.30
LTA-$Sr_{(8)}$ + $6H_2O$ + $Sr^{2+} \cdot (H_2O)_6 \rightarrow$ LTA-$2Sr_{(8)}$ + $2Na^+ \cdot (H_2O)_6$	-5.31
LTA-$2Sr_{(8)}$ + $6H_2O$ + $Sr^{2+} \cdot (H_2O)_6 \rightarrow$ LTA-$3Sr_{(8)}$ + $2Na^+ \cdot (H_2O)_6$	-5.76
LTA-$3Sr_{(8)}$ + $6H_2O$ + $Sr^{2+} \cdot (H_2O)_6 \rightarrow$ LTA-$4Sr_{(8)}$ + $2Na^+ \cdot (H_2O)_6$	-3.81
LTA-$4Sr_{(8)} \rightarrow$ LTA-$2Sr_{(6)}$-$2Sr_{(8)}$	-0.42
LTA-$4Sr_{(8)}$ + $6H_2O$ + $Sr^{2+} \cdot (H_2O)_6 \rightarrow$ LTA-$5Sr_{(8)}$ + $2Na^+ \cdot (H_2O)_6$	-2.85
LTA-$5Sr_{(8)}$ + $6H_2O$ + $Sr^{2+} \cdot (H_2O)_6 \rightarrow$ LTA-$6Sr_{(8)}$ + $2Na^+ \cdot (H_2O)_6$	-3.11
LTA-$2Sr_{(6)}$-$2Sr_{(8)}$ + $6H_2O$ + $Sr^{2+} \cdot (H_2O)_6 \rightarrow$ LTA-$4Sr_{(6)}$-$1Sr_{(8)}$ + $2Na^+ \cdot (H_2O)_6$	-2.69
LTA-$4Sr_{(6)}$-$1Sr_{(8)}$ + $6H_2O$ + $Sr^{2+} \cdot (H_2O)_6 \rightarrow$ LTA-$6Sr_{(6)}$ + $2Na^+ \cdot (H_2O)_6$	-2.69
LTA-$5Sr_{(8)} \rightarrow$ LTA-$4Sr_{(6)}$-$1Sr_{(8)}$	-0.26
LTA-$6Sr_{(8)} \rightarrow$ LTA-$6Sr_{(6)}$	-3.55

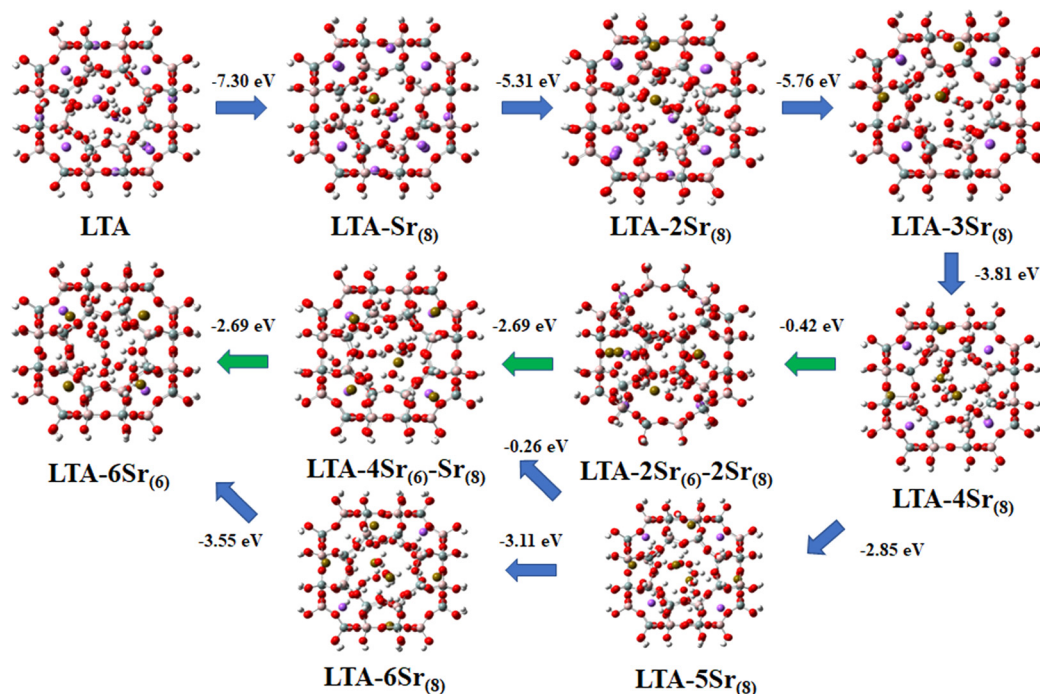**Fig. 8** Calculated ion-exchange energies of $Sr^{2+} \cdot (H_2O)_6$ into NaA zeolite and the corresponding pathway. The ion-exchange path labelled with the green arrows is the thermodynamically favourable path.

the *s8r*'s centers are dissociated (LTA-3Sr$_{(8)}$). The ion-exchange energy for this step is −5.76 eV. At this stage, all six Na$^+$ ions in the center of *s8r* are dissociated, leaving six empty *s8r* centers, with three of them occupied by Sr^{2+} ions. When the fourth Sr^{2+}·(H$_2$O)$_6$ is adsorbed by the empty *s8r* center, the two Na$^+$ ions at the center of *s6rs* will be dissociated (LTA-4Sr$_{(8)}$). Because Na$^+$ ions at *s6rs* center are more difficult to dissociate than Na$^+$ ions at the *s8r* center, the ion-exchange energy at this step is −3.81 eV, which is significantly less than those energies of the first three steps. The LTA-4Sr$_{(8)}$ has two types of vacancies: one is the two empty *s8rs*, and the other is the two empty *s6rs*. Additionally, we calculated another possibility: LTA-2Sr$_{(6)}$-2Sr$_{(8)}$, in which the fourth Sr^{2+} occupies one of the empty *s6r* when one Sr^{2+} was originally located at the center of *s8r* migrates to the other empty center of *s6r*. The potential energy with implicit solvation is further decreased by −0.42 eV, indicating that Sr^{2+} ions at the center of *s8r* can migrate to the *s6r* center during the ion-exchange process, while the fourth Sr^{2+} prefers an *s6r* center. Along with the ion-exchange of the fifth and the sixth Sr^{2+}·(H$_2$O)$_6$ ions, the Na$^+$ ions at the *s6rs* center are further removed, and it is expected that the empty *s6rs* center can be occupied by a new Sr^{2+} from solution, while the original Sr^{2+} migrates to the *s8r* center of the *lta*. Such a prediction is supported by the energy decreases of −2.69 eV for LTA-4Sr$_{(6)}$-1Sr$_{(8)}$ and −2.69 eV for LTA-6Sr$_{(6)}$. Because six *s8rs* are around the *lta* cage, the event of a fourth, fifth, and sixth Sr^{2+} being adsorbed at the empty center of *s8r* is also possible. Accordingly, we calculated the ion-exchange energies for the processes of LTA-4Sr$_{(8)}$ to LTA-5Sr$_{(8)}$ and further to LTA-6Sr$_{(8)}$, and the corresponding energy decreases are −2.85 and −3.11 eV, respectively.

DFT calculations indicate that migration of Sr^{2+} from the center of *s8r* to the unoccupied *s6r* center is always favourable. The energy decreases of LTA-5Sr$_{(8)}$ → LTA-4Sr$_{(6)}$-1Sr$_{(8)}$ and LTA-6Sr$_{(8)}$ → LTA-6Sr$_{(6)}$ are −0.26 and −3.55 eV, respectively. Considering that the process of LTA-4Sr$_{(8)}$ to LTA-2Sr$_{(6)}$-2Sr$_{(8)}$ is energy favourable, the rearrangement of ions within the *lta* cage should be easier than the ion-exchange process of LTA-4Sr$_{(8)}$ to LTA-5Sr$_{(8)}$. The ion-exchange path, labelled with green arrows in Fig. 8, represents the most feasible thermodynamic route, in which all six Sr^{2+} ions are finally located at the center of the *s6rs*. These predictions are consistent with the Rietveld refinements results showing the Sr^{2+} partially exchanged NaA (Fig. 4 and S2†).

3.5 Batch adsorptions

3.5.1 Sr^{2+} adsorption kinetics. The detailed adsorption data of NaA toward Sr^{2+} at different times are listed in Table S4.† We conducted the experiments three times. The average values from the first 5 minutes of mixing were used to perform the fitting. The adsorption kinetics of commercial NaA powder and irradiated commercial NaA powder for Sr^{2+} are depicted in Fig. 9. As presented in Fig. 9(a), the removal efficiencies of these two adsorbents rapidly increased to 89.23 ± 0.02% and 74.83 ± 2.25%, respectively, in the first 0.5 min. When further extending the contact time to 5 min, the
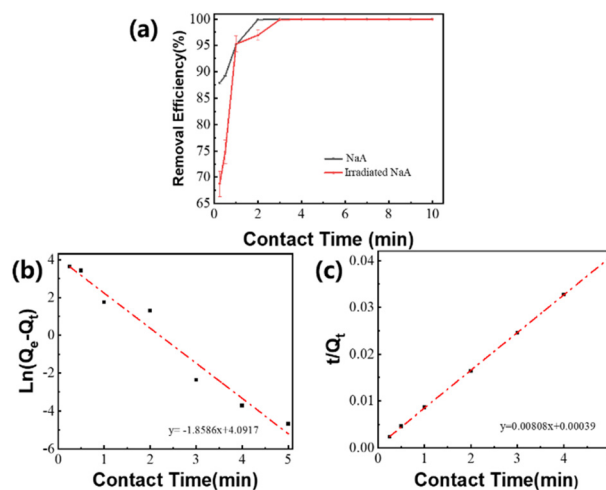

Fig. 9 (a) Adsorption kinetics of NaA and irradiated NaA for Sr^{2+}. (b) Linear fitting with the pseudo-first-order model and (c) the pseudo-second-order model for NaA zeolite.

removal efficiencies of the two adsorbents reached 99.96 ± 0.01%. The results in Fig. 9(a) suggest that the NaA has fast adsorption kinetics and excellent radiation resistance. As shown in Fig. 1(b), the water content physically adsorbed in NaA zeolite powder was 17.23 wt%, which will be considered in the following calculations on adsorption capacity. Fig. 9(b) and (c) show the linear fitting of the adsorption kinetics of both adsorbents with pseudo-first-order and the pseudo-second-order equations, respectively.

The equation of pseudo-first-order kinetics is:[24]

$$Q_t = Q_e(1 - e^{-K_1 t})$$

where Q_e is the equilibrium adsorption capacity in mg g^{-1}, Q_t is the amount absorbed in mg g^{-1} at time t in min, and K_1 (in min^{-1}) is the rate constant.

The pseudo-second-order kinetics equation is:[62]

$$\frac{t}{Q_t} = \frac{1}{k_2 Q_e{}^2} + \frac{t}{Q_e}$$

where Q_t (in mg g^{-1}) is the amount absorbed at time t in min, Q_e (in mg g^{-1}) is the equilibrium adsorption capacity, and k_2 [in g (mg min)$^{-1}$] is the rate constant.

The fitting result of the adsorption kinetics data with pseudo-first-order and pseudo-second-order kinetics models is shown in Fig. 9(b) and (c), respectively. The corresponding fitting parameters are presented in Table 4. The results in Table 4 indicate that the adsorption kinetics of NaA for Sr^{2+} is better described by the pseudo-second-order kinetics model than the pseudo-first-order model because the correlation coefficient of the former is 0.999, while that of the latter is 0.963.[63]

3.5.2 Sr^{2+} adsorption isotherms. The detailed adsorption data of NaA toward Sr^{2+} at different initial concentrations are listed in Table S5.† We conducted the experiments three times. The average values were used to perform the fitting. The

This journal is © the Partner Organisations 2022

Inorg. Chem. Front., 2022, **9**, 6258–6270 | **6265**

Table 4 Kinetic parameters for Sr^{2+} sorption in NaA zeolite

Pseudo-first-order model			Pseudo-second-order model		
R^2	Q_e (mg g^{-1})	K_1 (min^{-1})	R^2	Q_e (mg g^{-1})	k_2 (g (mg min)$^{-1}$)
0.963	90.352	1.86	0.999	123.761	0.167

adsorption isotherms of NaA for Sr^{2+} and the corresponding fitting with the Langmuir and the Freundlich models are shown in Fig. 10(a), (b), and (c), respectively. The fitting parameters are summarized in Table 5.
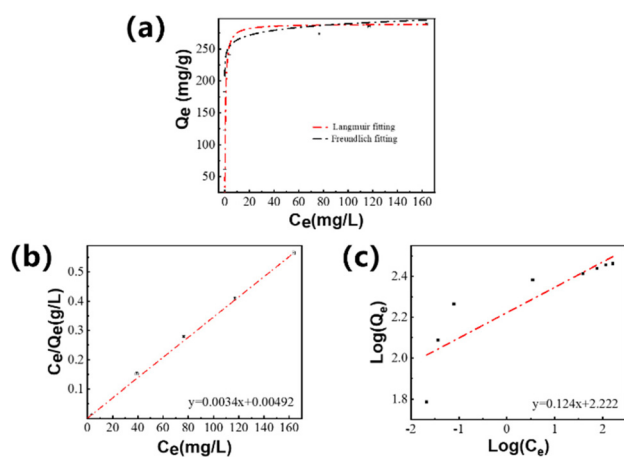
The Freundlich model equation is:[64]

$$Q_e = K_f C_e^{1/n}$$

where Q_e is the equilibrium adsorption capacity in mg g^{-1}, C_e is the concentration of Sr^{2+} in mg L^{-1} at equilibrium, and K_f (in mg$^{1-1/n}$ L$^{1/n}$ g^{-1}) and n are the parameters related to the adsorption capacity and the adsorption strength, respectively.

The Langmuir model equation is:[56]

$$Q_e = \frac{Q_m b C_e}{1 + b C_e}$$

where Q_m is the maximum equilibrium adsorption capacity in mg g^{-1}, C_e is the concentration of Sr^{2+} in mg L^{-1} at equilibrium, and b is a constant in L mg^{-1} related to the adsorption energy.

Fig. 10 (a) Adsorption isotherms of NaA. (b) Linear fitting with the Langmuir model and (c) the Freundlich model.

Table 5 Langmuir and Freundlich isotherm parameters for Sr^{2+} adsorption in NaA zeolite

Langmuir isotherm model			Freundlich isotherm model		
R^2	Q_m (mg g^{-1})	b (L mg^{-1})	R^2	$1/n$	K_f (mg$^{1-1/n}$ L$^{1/n}$ g^{-1})
0.998	294.12	0.691	0.757	0.125	166.72

The results in Fig. 10(b) and (c) and Table 5 indicate that the adsorption of Sr^{2+} in NaA follows the Langmuir model, suggesting a monolayer adsorption.[65] According to the Langmuir model, the calculated maximum adsorption capacity of NaA for Sr^{2+} is 294.12 mg g^{-1}, which is slightly lower than the theoretical adsorption capacity (308.52 mg g^{-1}) calculated based on the chemical composition. This result shows that Sr^{2+} can exchange almost all Na$^+$ ions.

3.5.3 Influence of dosage and pH. The detailed adsorption data of NaA toward Sr^{2+} at different pH values and adsorbent dosages are listed in Tables S6 and S7,† respectively. The influence of the dosage and the solution pH on the Sr^{2+} removal efficiency of NaA is shown in Fig. 11(a) and (b), respectively. As shown in Fig. 11(a), the removal efficiency increases with an increase of the solid/liquid ratios, suggesting that a higher concentration of adsorbent favors the removal of Sr^{2+}. The removal efficiency reaches 99.96 ± 0.01% at a solid/liquid ratio of 1 g L^{-1}. However, the adsorption capacity decreases with an increase in solid/liquid ratios. Such a phenomenon can be attributed to the fact that the adsorptive sites are excessive when increasing the adsorbent dosage. Therefore, choosing an optimal adsorbent dosage that can balance the removal efficiency and the adsorption capacity is important in practical applications. The data in Fig. 11(a) suggest that the solid/liquid ratio of 1 g L^{-1} can balance the adsorption efficiency and the adsorption capacity, which would be an appropriate solid/liquid ratio in practical applications. According to the solubility product of Sr(OH)$_2$ and given a Sr^{2+} concentration of 100 mg L^{-1}, precipitation will occur at pH 14.[66] Therefore, the initial pH of the solution is set no higher than 13 when investigating the influence of pH on the removal efficiency of NaA zeolite. Fig. 11(b) shows the Sr^{2+} removal efficiencies of NaA at pH values of 3–12 and a solid/liquid ratio of 1 g L^{-1}. The results in Fig. 11(b) indicate that the removal efficiency of NaA for Sr^{2+} is less affected within a wide pH range of 4–12 and the
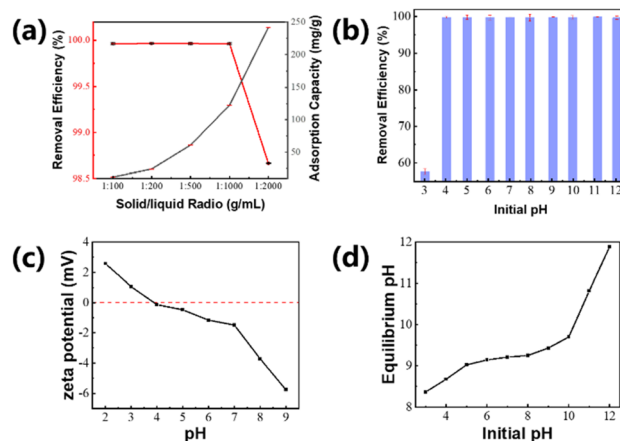
Fig. 11 (a) Sr^{2+} removal efficiency and adsorption capacity using NaA with various solid/liquid ratios. (b) Sr^{2+} removal efficiency of NaA at various initial solution pHs (the solid/liquid ratio is 1 g L^{-1}). (c) Zeta potential of NaA as a function of pH. (d) The initial pH and the corresponding equilibrium pH.

6266 | *Inorg. Chem. Front.*, 2022, **9**, 6258–6270

This journal is © the Partner Organisations 2022

removal efficiency is always greater than 99%. At the initial pH of 3, the removal efficiency of NaA for Sr^{2+} significantly dropped to 56.68 ± 0.68%, which can be attributed to the competition of H^+ and the positive charge of zeolite crystal surfaces. Fig. 11(c) shows the zeta potential of NaA as a function of pH, with pH 3 being very close to the point of zero charge (PZC) for silica and alumina, the main components of zeolites.[67] The results in Fig. 11(d) show that although the initial pH ranges from 3 to 8, the equilibrium pH values remain in a narrow range of 8.36 to 9.14. This also explains that, even when the pH value is 3, the zeta potential of NaA is positive, which ensures NaA still has the ability to adsorb strontium ions. These results indicate that NaA has an excellent acidic/basic buffer ability.

3.5.4 Selectivity. In practice, real low-level nuclear wastewater usually contains extremely low concentrations of $^{90}Sr^{2+}$ and high concentrations of competitive cations, such as Na^+, K^+, Ca^{2+}, and/or Mg^{2+}. Therefore, selectivity experiments were carried out by mixing Na^+, K^+, Mg^{2+}, Ca^{2+}, and Sr^{2+} at a concentration of 100 mg L^{-1} to investigate the selectivity of NaA zeolite toward Sr^{2+} at the same concentration and the results are shown in Fig. 12(a). As shown in Fig. 12(a), the removal efficiency of NaA for Sr^{2+} is the highest. Accompanying the adsorption or exchange-in of Sr^{2+}, Na^+ ions in NaA are exchanged-out, resulting in an increasing concentration of Na^+ ions in solution and a negative removal efficiency for Na^+. Furthermore, by mixing 100 mg L^{-1} of Sr^{2+} with different concentrations (0.1, 0.2, 0.3, 0.4 or 0.5 mol L^{-1}) of Na^+, K^+, Ca^{2+}, or Mg^{2+}, we investigated the influence of competitive cations on the Sr^{2+} removal efficiency of NaA. Fig. 12(b) shows the removal efficiency of NaA for Sr^{2+} as a function of the concentration of competitive cations.

As shown in Fig. 12(b), the adsorption of Sr^{2+} in NaA is less affected by Na^+ and Mg^{2+}, even when the cation concentration is as high as 0.5 M ($Na^+(Mg^{2+})/Sr^{2+}$ = 438/1), in which the removal efficiency is maintained above 80%. However, the adsorption of Sr^{2+} in NaA is very sensitive to the coexistence of K^+ and Ca^{2+}, especially Ca^{2+}. Even though the cation concentration is as low as 0.1 M (Ca^{2+}/Sr^{2+} = 88/1), the removal efficiency is decreased remarkably to below 20%. The removal efficiency of NaA for Sr^{2+} was greatly decreased from 93.17 ± 2.94% to 39.67 ± 3.07%, with the increase of the concentration of K^+ from 0.1 M to 0.5 M. These results suggest the removal of

K^+ and Ca^{2+} in the wastewater pretreatment stage is important for efficient Sr^{2+} removal.

4. Conclusions

NaA zeolite can capture trace level radioactive $^{90}Sr^{2+}$ (400 Bq L^{-1}, 7.75×10^{-2} ppt) from highly salted nuclear wastewater (0.03 M Na^+ and 0.4 M NH_4^+, $Na^+/^{90}Sr^{2+}$ = 3.48×10^{10}, and $NH_4^+/^{90}Sr^{2+}$ = 4.64×10^{11}). The distribution coefficient of K_d is as high as 421.56 ± 13.39 L g^{-1}. The structural Rietveld refinements of NaA-Sr samples reveal that all Sr^{2+} ions are located at the center of the *s6rs* of *lta* cages. The DFT calculations indicate that the Na^+ at the center of *s8r* is first replaced by Sr^{2+}, and then the Sr^{2+} at the center of *s8r* migrates to the center of *s6r* when it is available. Along with the ion-exchange process, all Sr^{2+} ions at the center of *s8rs* migrate to the center of *s6rs*. Compared with ions of NH_4^+, K^+, Cs^+, Mg^{2+}, and Ca^{2+}, the replacement of Na^+ with Sr^{2+} has the lowest energy, which explains the exceptionally high selectivity of NaA zeolite in extracting the radioactive isotope of $^{90}Sr^{2+}$. Meanwhile, NaA zeolite exhibits rapid adsorption kinetics (about 5 minutes), high capture capacity (294.12 mg g^{-1}), a broad operating pH range (4–12), and strong radiation resistance when extracting Sr^{2+} from solution. These superior features, together with its ultra-low cost and environmentally benign nature, make NaA zeolite a promising candidate for nuclear wastewater management.

Conflicts of interest
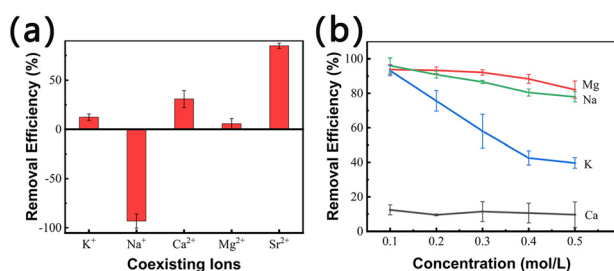
There are no conflicts to declare.

Acknowledgements

Fig. 12 (a) Removal efficiency of NaA for Na^+, K^+, Ca^{2+}, Mg^{2+}, and Sr^{2+} in a mixed solution, $C_{0(M^{n+})}$ = 100 ppm. (b) Influence of competitive cations of Na^+, K^+, Ca^{2+}, and Mg^{2+} on Sr^{2+} adsorption in NaA zeolite.

References

1 D. Alby, C. Charnay, M. Heran, B. Prelot and J. Zajac, Recent developments in nanostructured inorganic materials for sorption of cesium and strontium: Synthesis and shaping, sorption capacity, mechanisms, and selectivity-A review, *J. Hazard. Mater.*, 2018, **344**, 511–530.

2 L. Xu and J. Wang, The application of graphene-based materials for the removal of heavy metals and radionuclides from water and wastewater, *Crit. Rev. Environ. Sci. Technol.*, 2017, **47**, 1042–1105.

3 S. K. Sahoo, N. Kavasi, A. Sorimachi, H. Arae, S. Tokonami, J. W. Mietelski, E. Lokas and S. Yoshida, Strontium-90 activity concentration in soil samples from the exclusion zone of the Fukushima daiichi nuclear power plant, *Sci. Rep.*, 2016, **6**, 23925.

4 R. J. Konings, T. Wiss and O. Benes, Predicting material release during a nuclear reactor accident, *Nat. Mater.*, 2015, **14**, 247–252.

5 J. Zhou, S. Hao, L. Gao and Y. Zhang, Study on adsorption performance of coal based activated carbon to radioactive iodine and stable iodine, *Ann. Nucl. Energy*, 2014, **72**, 237–241.

6 F. Guo, Z. Zhu, Z. Zheng, Y. Jin, X. Di, Z. Xu and H. Guan, Facile synthesis of highly efficient fluorescent carbon dots for tetracycline detection, *Environ. Sci. Pollut. Res. Int.*, 2020, **27**, 4520–4527.

7 S. Chitra, S. Viswanathan, S. V. S. Rao and P. K. Sinha, Uptake of cesium and strontium by crystalline silicotitanates from radioactive wastes, *J. Radioanal. Nucl. Chem.*, 2010, **287**, 955–960.

8 M. B. Chadwick, M. Herman, P. Obložinský, M. E. Dunn, Y. Danon, A. C. Kahler, D. L. Smith, B. Pritychenko, G. Arbanas, R. Arcilla, R. Brewer, D. A. Brown, R. Capote, A. D. Carlson, Y. S. Cho, H. Derrien, K. Guber, G. M. Hale, S. Hoblit, S. Holloway, T. D. Johnson, T. Kawano, B. C. Kiedrowski, H. Kim, S. Kunieda, N. M. Larson, L. Leal, J. P. Lestone, R. C. Little, E. A. McCutchan, R. E. MacFarlane, M. MacInnes, C. M. Mattoon, R. D. McKnight, S. F. Mughabghab, G. P. A. Nobre, G. Palmiotti, A. Palumbo, M. T. Pigni, V. G. Pronyaev, R. O. Sayer, A. A. Sonzogni, N. C. Summers, P. Talou, I. J. Thompson, A. Trkov, R. L. Vogt, S. C. van der Marck, A. Wallner, M. C. White, D. Wiarda and P. G. Young, ENDF/B-VII.1 Nuclear Data for Science and Technology: Cross Sections, Covariances, Fission Product Yields and Decay Data, *Nucl. Data Sheets*, 2011, **112**, 2887–2996.

9 S. J. Datta, P. Oleynikov, W. K. Moon, Y. Ma, A. Mayoral, H. Kim, C. Dejoie, M. K. Song, O. Terasaki and K. B. Yoon, Removal of ^{90}Sr from highly Na^+-rich liquid nuclear waste with a layered vanadosilicate, *Energy Environ. Sci.*, 2019, **12**, 1857–1865.

10 B. Hu, Q. Hu, D. Xu and C. Chen, The adsorption of U(VI) on carbonaceous nanofibers: A combined batch, EXAFS and modeling techniques, *Sep. Purif. Technol.*, 2017, **175**, 140–146.

11 S. J. Ahmadi, N. Akbari, Z. Shiri-Yekta, M. H. Mashhadizadeh and A. Pourmatin, Adsorption of strontium ions from aqueous solution using hydrous, amorphous MnO_2–ZrO_2 composite: a new inorganic ion exchanger, *J. Radioanal. Nucl. Chem.*, 2013, **299**, 1701–1707.

12 I. M. M. Rahman, Y. Ye, M. F. Alam, H. Sawai, Z. A. Begum, Y. Furusho, A. Ohta and H. Hasegawa, Selective Separation of Radiocesium from Complex Aqueous Matrices Using Dual Solid-Phase Extraction Systems, *J. Chromatogr. A*, 2021, **1654**, 462476.

13 T. Sun, Z. Zheng, J. Chen, J. Wang and C. Xu, Efficient co-extraction of strontium and cesium from nitric acid medium by mixtures of di-tert-butylcyclohexano-18-crown-6 and 1,3-di(2-propoxy)calix[4]arene-crown-6 in n-octanol, *Sep. Sci. Technol.*, 2017, **53**, 503–512.

14 D. R. Raut and P. K. Mohapatra, Simultaneous extraction of Cs and Sr from synthetic high level waste solutions using a solvent containing chlorinated dicarbollide and PEG-400 in PTMS, *J. Radioanal. Nucl. Chem.*, 2013, **299**, 75–80.

15 D. J. Hodkin, D. I. Stewart, J. T. Graham and I. T. Burke, Coprecipitation of (14)C and Sr with carbonate precipitates: The importance of reaction kinetics and recrystallization pathways, *Sci. Total Environ.*, 2016, **562**, 335–343.

16 N. Meunier, P. Drogui, C. Montane, R. Hausler, G. Mercier and J. F. Blais, Comparison between electrocoagulation and chemical precipitation for metals removal from acidic soil leachate, *J. Hazard. Mater.*, 2006, **137**, 581–590.

17 L. Zhang, Y. Lu, Y. L. Liu, M. Li, H. Y. Zhao and L. A. Hou, High flux MWCNTs-interlinked GO hybrid membranes survived in cross-flow filtration for the treatment of strontium-containing wastewater, *J. Hazard. Mater.*, 2016, **320**, 187–193.

18 N. Combernoux, L. Schrive, V. Labed, Y. Wyart, E. Carretier and P. Moulin, Treatment of radioactive liquid effluents by reverse osmosis membranes: From lab-scale to pilot-scale, *Water Res.*, 2017, **123**, 311–320.

19 Y. Yin, J. Wang, X. Yang and W. Li, Removal of Strontium Ions by Immobilized Saccharomyces Cerevisiae in Magnetic Chitosan Microspheres, *Nucl. Eng. Technol.*, 2017, **49**, 172–177.

20 T. Sun, L. Xu, D. Wang and Y. Li, Metal organic frameworks derived single atom catalysts for electrocatalytic energy conversion, *Nano Res.*, 2019, **12**, 2067–2080.

21 M. J. Manos and M. G. Kanatzidis, Metal sulfide ion exchangers: superior sorbents for the capture of toxic and nuclear waste-related metal ions, *Chem. Sci.*, 2016, 7, 4804–4824.

22 X. H. Xiong, Z. W. Yu, L. L. Gong, Y. Tao, Z. Gao, L. Wang, W. H. Yin, L. X. Yang and F. Luo, Ammoniating Covalent Organic Framework (COF) for High-Performance and Selective Extraction of Toxic and Radioactive Uranium Ions, *Adv. Sci.*, 2019, **6**, 1900547.

23 M. Wang, F. Huang, C. Wang, Y. Hu, P. Wu, A. Hu, J. Ji and J. Wang, Synthesis of a bimetallic metal–organic framework catalyst via selective detection and adsorption of Fe^{3+} for

6268 | *Inorg. Chem. Front.*, 2022, **9**, 6258–6270

This journal is © the Partner Organisations 2022

enhanced bio-based catalysis, *Inorg. Chem. Front.*, 2021, **8**, 4998–5005.

24 B. Wang, J. Li, X. Zhou, W. Hao, S. Zhang, C. Lan, X. Wang, Z. Wang, J. Xu, J.-N. Zhang, X. Li and W. Yan, Facile activation of lithium slag for the hydrothermal synthesis of zeolite A with commercial quality and high removal efficiency for the isotope of radioactive ^{90}Sr, *Inorg. Chem. Front.*, 2022, **9**, 468–477.

25 D. Gao, X. Yu, Y. Guo, S. Wang, M. Liu, T. Deng, Y. Chen and N. Belzile, Extraction of lithium from salt lake brine with triisobutyl phosphate in ionic liquid and kerosene, *Chem. Res. Chin. Univ.*, 2015, **31**, 621–626.

26 J. Zhang, J. Liu, Y. Liu, Y. Wang, Q. Fang and S. Qiu, A Two-dimensional Covalent Organic Framework for Iodine Adsorption, *Chem. Res. Chin. Univ.*, 2022, **38**, 456–460.

27 J. T. T. Foster, Y. Hu and T. H. Boyer, Affinity of potassium-form cation exchange resin for alkaline earth and transition metals, *Sep. Purif. Technol.*, 2017, **175**, 229–237.

28 T. Nur, P. Loganathan, J. Kandasamy and S. Vigneswaran, Removal of strontium from aqueous solutions and synthetic seawater using resorcinol formaldehyde polycondensate resin, *Desalination*, 2017, **420**, 283–291.

29 S. Chegrouche, A. Mellah and M. Barkat, Removal of strontium from aqueous solutions by adsorption onto activated carbon: kinetic and thermodynamic studies, *Desalination*, 2009, **235**, 306–318.

30 Z. Nie, N. Finck, F. Heberling, T. Pruessmann, C. Liu and J. Lutzenkirchen, Adsorption of Selenium and Strontium on Goethite: EXAFS Study and Surface Complexation Modeling of the Ternary Systems, *Environ. Sci. Technol.*, 2017, **51**, 3751–3758.

31 M. Ghaly, F. M. S. E. El-Dars, M. M. Hegazy and R. O. Abdel Rahman, Evaluation of synthetic Birnessite utilization as a sorbent for cobalt and strontium removal from aqueous solution, *Chem. Eng. J.*, 2016, **284**, 1373–1385.

32 J. Liang, J. Li, X. Li, K. Liu, L. Wu and G. Shan, The sorption behavior of CHA-type zeolite for removing radioactive strontium from aqueous solutions, *Sep. Purif. Technol.*, 2020, **230**, 115874.

33 I. Smiciklas, I. Coha, M. Jovic, M. Nodilo, M. Sljivic-Ivanovic, S. Smiljanic and Z. Grahek, Efficient separation of strontium radionuclides from high-salinity wastewater by zeolite 4A synthesized from Bayer process liquids, *Sci. Rep.*, 2021, **11**, 1738.

34 G. Li, G. Ji, W. Liu, J. Zhang, L. Song, L. Cheng, X. Wang, Y. Wang, J. Liu, X. Chen, X. Sun and J. Diwu, A hydrolytically stable anionic layered indium-organic framework for the efficient removal of (90)Sr from seawater, *Dalton Trans.*, 2019, **48**, 17858–17863.

35 W. Mu, S. Du, X. Li, Q. Yu, R. Hu, H. Wei, Y. Yang and S. Peng, Efficient and irreversible capture of strontium ions from aqueous solution using metal-organic frameworks with ion trapping groups, *Dalton Trans.*, 2019, **48**, 3284–3290.

36 M. Hao, Z. Chen, X. Liu, X. Liu, J. Zhang, H. Yang, G. I. N. Waterhouse, X. Wang and S. Ma, Converging Cooperative Functions into the Nanospace of Covalent Organic Frameworks for Efficient Uranium Extraction from Seawater, *CCS Chem.*, 2022, **4**, 2294–2307.

37 Y. Kakutani, P. Weerachawanasak, Y. Hirata, M. Sano, T. Suzuki and T. Miyake, Highly effective K-Merlinoite adsorbent for removal of Cs^+ and Sr^{2+} in aqueous solution, *RSC Adv.*, 2017, **7**, 30919–30928.

38 M. R. Awual, T. Yaita, T. Taguchi, H. Shiwaku, S. Suzuki and Y. Okamoto, Selective cesium removal from radioactive liquid waste by crown ether immobilized new class conjugate adsorbent, *J. Hazard. Mater.*, 2014, **278**, 227–235.

39 S. Kwon, C. Kim, E. Han, H. Lee, H. S. Cho and M. Choi, Relationship between zeolite structure and capture capability for radioactive cesium and strontium, *J. Hazard. Mater.*, 2021, **408**, 124419.

40 X. Yang, D. Albrecht and J. Caro, Revision of Charnell's procedure towards the synthesis of large and uniform crystals of zeolites A and X, *Microporous Mesoporous Mater.*, 2006, **90**, 53–61.

41 G. Kresse and J. Hafner, Ab initio molecular dynamics for liquid metals, *Phys. Rev. B: Condens. Matter Mater. Phys.*, 1993, **47**, 558–561.

42 G. Kresse and J. Furthmüller, Efficient iterative schemes for ab initio total-energy calculations using a plane-wave basis set, *Phys. Rev. B: Condens. Matter Mater. Phys.*, 1996, **54**, 11169.

43 J. P. Perdew, K. Burke and M. Ernzerhof, Generalized Gradient Approximation Made Simple, *Phys. Rev. Lett.*, 1996, **77**, 3865–3868.

44 S. Grimme, J. Antony, S. Ehrlich and H. Krieg, A consistent and accurate ab initio parametrization of density functional dispersion correction (DFT-D) for the 94 elements H-Pu, *J. Chem. Phys.*, 2010, **132**, 154104.

45 G. Kresse and D. Joubert, From ultrasoft pseudopotentials to the projector augmented-wave method, *Phys. Rev. B: Condens. Matter Mater. Phys.*, 1999, **59**, 1758.

46 P. E. Blöchl, Projector augmented-wave method, *Phys. Rev. B: Condens. Matter Mater. Phys.*, 1994, **50**, 17953–17979.

47 M. J. Frisch, G. W. Trucks, H. B. Schlegel, G. E. Scuseria, M. A. Robb, J. R. Cheeseman, G. Scalmani, V. Barone, G. A. Petersson, H. Nakatsuji, X. Li, M. Caricato, A. V. Marenich, J. Bloino, B. G. Janesko, R. Gomperts, B. Mennucci, H. P. Hratchian, J. V. Ortiz, A. F. Izmaylov, J. L. Sonnenberg, D. Williams-Young, F. Ding, F. Lipparini, F. Egidi, J. Goings, B. Peng, A. Petrone, T. Henderson, D. Ranasinghe, V. G. Zakrzewski, J. Gao, N. Rega, G. Zheng, W. Liang, M. Hada, M. Ehara, K. Toyota, R. Fukuda, J. Hasegawa, M. Ishida, T. Nakajima, Y. Honda, O. Kitao, H. Nakai, T. Vreven, K. Throssell, J. A. Montgomery, Jr., J. E. Peralta, F. Ogliaro, M. J. Bearpark, J. J. Heyd, E. N. Brothers, K. N. Kudin, V. N. Staroverov, T. A. Keith, R. Kobayashi, J. Normand, K. Raghavachari, A. P. Rendell, J. C. Burant, S. S. Iyengar, J. Tomasi, M. Cossi, J. M. Millam, M. Klene, C. Adamo, R. Cammi, J. W. Ochterski, R. L. Martin, K. Morokuma, O. Farkas, J. B. Foresman and D. J. Fox, *Gaussian* 16, Revision A.03, Gaussian, Inc., Wallingford CT, 2016.

This journal is © the Partner Organisations 2022

Inorg. Chem. Front., 2022, **9**, 6258–6270 | **6269**

48 A. D. Becke, Density-functional thermochemistry. III. The role of exact exchange, *J. Phys. Chem. C*, 1993, **98**, 5648–5652.

49 A. V. Marenich, C. J. Cramer and D. G. Truhlar, Universal Solvation Model Based on Solute Electron Density and on a Continuum Model of the Solvent Defined by the Bulk Dielectric Constant and Atomic Surface Tensions, *J. Phys. Chem. B*, 2009, **113**, 6378–6396.

50 M. H. F. Sluiter and Y. Kawazoe, Prediction of the mixing enthalpy of alloys, *Europhys. Lett.*, 2002, **57**, 526–5532.

51 V. L. Vinograd, M. H. F. Sluiter and B. Winkler, , Subsolidus phase relations in theCaCO$_3$–MgCO3 system predicted from the excess enthalpies of supercell structures with single and double defects, *Phys. Rev. B: Condens. Matter Mater. Phys.*, 2009, **79**, 104201.

52 T. B. Reed and D. W. Breck, Crystalline Zeolites. II. Crystal Structure of Synthetic Zeolite, Type A, *J. Am. Chem. Soc.*, 1956, **78**, 5972–5977.

53 V. Grämlich and W. M. Meier, The crystal structure of hydrated NaA: A detailed refinement of a pseudosymmetric zeolite structure, *Z. Kristallogr. - Cryst. Mater.*, 1971, **133**, 134–149.

54 H. Kistenmacher, H. Popkie and E. Clementi, Study of the structure of molecular complexes. VIII. Small clusters of water molecules surrounding Li$^+$, Na$^+$, K$^+$, F$^-$, and Cl$^-$ ions, *J. Chem. Phys.*, 1974, **61**, 799–815.

55 M. Peschke, A. T. Blades and P. Kebarle, Hydration Energies and Entropies for Mg^{2+},Ca^{2+},Sr^{2+}, and Ba^{2+} from Gas-Phase Ion-Water Molecule Equilibria Determinations, *J. Phys. Chem. A*, 1998, **102**, 9978–9985.

56 Y. Wang, P. Bai, Z. Jin, Y. Li, A. Yaorui Li, W. Shi, J. Xu, W. Yan and R. Xu, Stellerite-seeded facile synthesis of zeolite heulandite with exceptional aqueous Cd^{2+} capture performance, *Inorg. Chem. Front.*, 2019, **6**, 1785–1792.

57 A. Merceille, E. Weinzaepfel, Y. Barré and A. Grandjean, The sorption behaviour of synthetic sodium nonatitanate and zeolite A for removing radioactive strontium from aqueous wastes, *Sep. Purif. Technol.*, 2012, **96**, 81–88.

58 C. Liu, L. Chen, Z. Ye, C. Li, X. Yin, X. Wang and Y. Wei, Pellet silica-based titanate adsorbents with high selectivity for strontium removal from synthetic radioactive solutions, *J. Sol-Gel Sci. Technol.*, 2019, **91**, 273–285.

59 Z. Chen, Y. Wu, Y. Wei and H. Mimura, Preparation of silica-based titanate adsorbents and application for strontium removal from radioactive contaminated wastewater, *J. Radioanal. Nucl. Chem.*, 2015, **307**, 931–940.

60 A. Sachse, A. Merceille, Y. Barré, A. Grandjean, F. Fajula and A. Galarneau, Macroporous LTA-monoliths for in-flow removal of radioactive strontium from aqueous effluents: Application to the case of Fukushima, *Microporous Mesoporous Mater.*, 2012, **164**, 251–258.

61 M. Peschke, A. T. Blades and P. Kebarle, Binding Energies for Doubly-Charged Ions M^{2+} = Mg^{2+}, Ca^{2+} and Zn^{2+} with the Ligands L =H$_2$O, Acetone and N-methylacetamide in Complexes MLn^{2+} for n = 1 to 7 from Gas Phase Equilibria Determinations and Theoretical Calculations, *J. Am. Chem. Soc.*, 2000, **122**, 10440–10449.

62 Y. Li, P. Bai, Y. Yan, W. Yan, W. Shi and R. Xu, Removal of Zn^{2+}, Pb^{2+}, Cd^{2+}, and Cu^{2+} from aqueous solution by synthetic clinoptilolite, *Microporous Mesoporous Mater.*, 2019, **273**, 203–211.

63 Y. Li, B. Pan, H. Miao, H. Xu, X. Liu and G. Shi, Single and Binary Dye Adsorption of Methylene Blue and Methyl Orange in Alcohol Aqueous Solution via Rice Husk Based Activated Carbon: Kinetics and Equilibrium Studies, *Chem. Res. Chin. Univ.*, 2020, **36**, 1272–1278.

64 P. Bai, Z. Dong, S. Wang, X. Wang, Y. Li, Y. Wang, Y. Ma, W. Yan, X. Zou and J. Yu, A Layered Cationic Aluminum Oxyhydroxide as a Highly Efficient and Selective Trap for Heavy Metal Oxyanions, *Angew. Chem., Int. Ed.*, 2020, **59**, 19539–19544.

65 W. Li, Y. Li, J. Liu, S. Chao, T. Yang, L. Li, C. Wang and X. Li, A Novel Hollow Carbon@MnO$_2$ Electrospun Nanofiber Adsorbent for Efficient Removal of Pb^{2+} in Wastewater, *Chem. Res. Chin. Univ.*, 2021, **37**, 496–504.

66 J. G. Speight, *Lange's Handbook of Chemistry*, McGraw-Hill, Inc., CD&W Inc., Laramie, Wyoming, 2005.

67 M. Kosmulski, *Surface Charging and Points of Zero Charge*, CRC Press, Boca Raton, 2009.

6270 | *Inorg. Chem. Front.*, 2022, **9**, 6258–6270

This journal is © the Partner Organisations 2022